Research Article | Vol. 25, No. 22 | 30 Oct 2017 | OPTICS EXPRESS 27624
Optics EXPRESS

Visible light nearly perfect absorber: an optimum unit cell arrangement for near absolute polarization insensitivity

AMIR GHOBADI,[1,2] HODJAT HAJIAN,[1] MURAT GOKBAYRAK,[1] SINA ABEDINI DERESHGI,[1,2] AHMET TOPRAK,[1] BAYRAM BUTUN,[1] AND EKMEL OZBAY[1,2,3,4,*]

[1]*NANOTAM-Nanotechnology Research Center, Bilkent University, 06800 Ankara, Turkey*
[2]*Department of Electrical and Electronics Engineering, Bilkent University, 06800 Ankara, Turkey*
[3]*Department of Physics, Bilkent University, 06800 Ankara, Turkey*
[4]*UNAM-Institute of Materials Science and Nanotechnology, Bilkent University, Ankara, Turkey*
**ozbay@bilkent.edu.tr*

Abstract: In this work, we propose an optimum unit cell arrangement to obtain near absolute polarization insensitivity in a metal-insulator-metal (MIM) based ultra-broadband perfect absorber. Our findings prove that upon utilizing this optimum arrangement, the response of the absorber is retained and unchanged over all arbitrary incidence light polarizations, regardless of the shape of the top metal patch. First, the impact of the geometry of the top nanopatch resonators on the absorption bandwidth of the overall structure is explored. Then, the response of the MIM design for different incidence polarizations and angles is scrutinized. Finally, the proposed design is fabricated and characterized.

© 2017 Optical Society of America

OCIS codes: (160.3918) Metamaterials; (310.6628) Subwavelength structures, nanostructures; (160.4760) Optical properties.

References and links

1. S. Luo, J. Zhao, D. Zuo, and X. Wang, "Perfect narrow band absorber for sensing applications," Opt. Express **24**(9), 9288–9294 (2016).
2. S. A. O. Olson, D. A. Mohr, J. Shaver, T. W. Johnson, and S. Oh, "Plasmonic Cup Resonators for Single-Nanohole-Based Sensing and Spectroscopy," ACS Photonics **3**, 1202–1207 (2016).
3. Y. Li, L. Su, C. Shou, C. Yu, J. Deng, and Y. Fang, "Surface-enhanced molecular spectroscopy (SEMS) based on perfect-absorber metamaterials in the mid-infrared," Sci. Rep. **3**, 2865 (2013).
4. J. O. Arroyo and P. Kukura, "Non-fluorescent schemes for single-molecule detection, imaging and spectroscopy," Nat. Photonics **10**, 11–17 (2016).
5. V. G. Kravets, F. Schedin, R. Jalil, L. Britnell, R. V. Gorbachev, D. Ansell, B. Thackray, K. S. Novoselov, A. K. Geim, A. V. Kabashin, and A. N. Grigorenko, "Singular phase nano-optics in plasmonic metamaterials for label-free single-molecule detection," Nat. Mater. **12**(4), 304–309 (2013).
6. S. A. Dereshgi, Z. Sisman, K. Topalli, and A. K. Okyay, "Plasmonically enhanced metal – insulator multistacked photodetectors with separate absorption and collection junctions for near-infrared applications," Sci. Rep. **7**, 42349 (2017).
7. H. Chalabi, D. Schoen, and M. L. Brongersma, "Hot-Electron Photodetection with a Plasmonic Nanostripe Antenna," Nano Lett. **14**(3), 1374–1380 (2014).
8. H. A. Atwater and A. Polman, "Plasmonics for improved photovoltaic devices," Nat. Mater. **9**(3), 205–213 (2010).
9. N. I. Landy, S. Sajuyigbe, J. J. Mock, D. R. Smith, and W. J. Padilla, "Perfect Metamaterial Absorber," Phys. Rev. Lett. **100**(20), 207402 (2008).
10. W. S. Chang, J. W. Ha, L. S. Slaughter, and S. Link, "Plasmonic nanorod absorbers as orientation sensors," Proc. Natl. Acad. Sci. U.S.A. **107**(7), 2781–2786 (2010).
11. Y. Avitzour, Y. A. Urzhumov, and G. Shvets, "Wide-angle infrared absorber based on a negative-index plasmonic metamaterial," Phys. Rev. B **79**, 1–5 (2009).
12. H. Tao, C. M. Bingham, D. Pilon, K. Fan, A. C. Strikwerda, D. Shrekenhamer, and W. J. Padilla, "A dual band terahertz metamaterial absorber," J. Phys. D Appl. Phys. **43**, 225102 (2010).
13. Q. Y. Wen, Y. S. Xie, H. W. Zhang, Q. H. Yang, Y. X. Li, and Y. L. Liu, "Transmission line model and fields analysis of metamaterial absorber in the terahertz band," Opt. Express **17**(22), 20256–20265 (2009).
14. N. Liu, M. Mesch, T. Weiss, M. Hentschel, and H. Giessen, "Infrared perfect absorber and its application as

#302933 https://doi.org/10.1364/OE.25.027624
Journal © 2017 Received 28 Jul 2017; revised 25 Sep 2017; accepted 19 Oct 2017; published 25 Oct 2017

Optics EXPRESS

plasmonic sensor," Nano Lett. **10**(7), 2342–2348 (2010).
15. J. Hao, J. Wang, X. Liu, W. J. Padilla, L. Zhou, and M. Qiu, "High performance optical absorber based on a plasmonic metamaterial," Appl. Phys. Lett. **96**, 251104 (2010).
16. M. Yan, "Metal-insulator-metal light absorber: a continuous structure," J. Opt. **15**, 25006 (2013).
17. N. Mattiucci, M. J. Bloemer, N. Aközbek, and G. D'Aguanno, "Impedance matched thin metamaterials make metals absorbing," Sci. Rep. **3**, 3203 (2013).
18. M. Chirumamilla, A. S. Roberts, F. Ding, D. Wang, P. K. Kristensen, S. I. Bozhevolnyi, and K. Pedersen, "Multilayer tungsten-alumina-based broadband light absorbers for high- temperature applications," Opt. Mater. Express **6**, 1443–1447 (2016).
19. H. Deng, Z. Li, L. Stan, D. Rosenmann, D. Czaplewski, J. Gao, and X. Yang, "Broadband perfect absorber based on one ultrathin layer of refractory metal," Opt. Lett. **40**(11), 2592–2595 (2015).
20. A. Ghobadi, S. A. Dereshgi, H. Hajian, B. Bozok, B. Butun, and E. Ozbay, "Ultra-broadband, wide angle absorber utilizing metal insulator multilayers stack with a multi-thickness metal surface texture," Sci. Rep. **7**(1), 4755 (2017).
21. K. Aydin, V. E. Ferry, R. M. Briggs, and H. A. Atwater, "Broadband polarization-independent resonant light absorption using ultrathin plasmonic super absorbers," Nat. Commun. **2**, 517 (2011).
22. X. Tian and Z. Li, "Visible-near infrared ultra-broadband polarization-independent metamaterial perfect absorber involving phase-change materials," Photonic Res. **4**, 146–152 (2016).
23. X. Ming and Q. Tan, "Design Method of a Broadband Wide-Angle Plasmonic Absorber in the Visible Range," Plasmonics **12**, 14–17 (2017).
24. H. Wang and L. Wang, "Perfect selective metamaterial solar absorbers," Opt. Express **21**, A1078–A1093 (2013).
25. F. Ding, J. Dai, Y. Chen, J. Zhu, Y. Jin, and S. I. Bozhevolnyi, "Broadband near-infrared metamaterial absorbers utilizing highly lossy metals," Sci. Rep. **6**, 39445 (2016).
26. M. G. Nielsen, A. Pors, O. Albrektsen, and S. I. Bozhevolnyi, "Efficient absorption of visible radiation by gap plasmon resonators," Opt. Express **20**(12), 13311–13319 (2012).
27. D. Hu, H.-Y. Wang, and Q.-F. Zhu, "Design of an ultra-broadband and polarization-insensitive solar absorber using a circular-shaped ring resonator," J. Nanophotonics **10**, 26021 (2016).
28. T. Søndergaard, S. M. Novikov, T. Holmgaard, R. L. Eriksen, J. Beermann, Z. Han, K. Pedersen, and S. I. Bozhevolnyi, "Plasmonic black gold by adiabatic nanofocusing and absorption of light in ultra-sharp convex grooves," Nat. Commun. **3**, 969 (2012).
29. G. Tagliabue, H. Eghlidi, and D. Poulikakos, "Facile multifunctional plasmonic sunlight harvesting with tapered triangle nanopatterning of thin films," Nanoscale **5**(20), 9957–9962 (2013).
30. Lumerical Solut, Inc. http://www.lumerical.com/tcad-products/fdtd/.
31. Y. Huang, X. Zhang, J. Li, L. Ma, and Z. Zhang, "Analytical plasmon dispersion in subwavelength closely spaced Au nanorod arrays from planar metal – insulator – metal waveguides," J. Mater. Chem. C Mater. Opt. Electron. Devices **5**, 6079–6085 (2017).
32. Y. Huang, L. Ma, M. Hou, and Z. Zhang, "Universal Near-Field Interference Patterns of Fano Resonances in Two-Dimensional Plasmonic Crystals," Plasmonics **11**, 1377–1383 (2016).
33. R. Nicolas, G. Lévêque, J. Marae-Djouda, G. Montay, Y. Madi, J. Plain, Z. Herro, M. Kazan, P. M. Adam, and T. Maurer, "Plasmonic mode interferences and Fano resonances in Metal-Insulator-Metal nanostructured interface," Sci. Rep. **5**, 14419 (2015).
34. Y. Francescato, V. Giannini, and S. A. Maier, "Plasmonic Systems Unveiled by Fano Resonances," ACS Nano **6**(2), 1830–1838 (2012).
35. M. Khorasaninejad, S. Mohsen Raeis-Zadeh, H. Amarloo, N. Abedzadeh, S. Safavi-Naeini, and S. S. Saini, "Colorimetric sensors using nano-patch surface plasmon resonators," Nanotechnology **24**(35), 355501 (2013).
36. M. G. Nielsen, D. K. Gramotnev, A. Pors, O. Albrektsen, and S. I. Bozhevolnyi, "Continuous layer gap plasmon resonators," Opt. Express **19**(20), 19310–19322 (2011).

1. Introduction

The fields of nanophotonics, near-field optics, and plasmonics all seek to harness light at subwavelength scales. The prospect of deep subwavelength light confinement is offered by plasmonics. The attributes of light harvesting and concentrating its energy into subwavelength volumes open a door for a variety of applications, including sensing and spectroscopy [1–3], single molecule detection [4,5], photo detection [6,7], and photovoltaics [8]. Generally, the main features for a perfect plasmonic absorber are the operation bandwidth, sensitivity to light polarization, omni-directionality, and for some applications the overall thickness of the design. In one of the first studies in this field, Landy *et al.* proposed a single wavelength perfect absorber based on a metallic split ring resonator [9]. To improve the performance of the plasmonic absorber, other architectures were later introduced [10–13]. However, due to a lack of trapping and confinement mechanisms, these ultrathin single plasmonic layers had an inherently low absorption capacity and could absorb only a fraction of the incoming light.

Optics EXPRESS

This restriction was later mitigated by introducing a metallic back reflecting layer that acted as an ideal mirror, reflecting the whole light spectrum [14–16]. In this configuration, a metal-insulator-metal (MIM) cavity can then be employed to trap light inside the design and consequently absorption near unity can be attained. As its name implies, MIM is mainly comprised of three distinct layers; 1) a bottom thick continuous metal layer, 2) a thin insulator spacing layer, and 3) a plasmonic subwavelength top metal patch. The absorption in this configuration is governed by the excitation of cavity modes originated from the coupling between the upper and lower metal-insulator surface plasmons. However, most of the above mentioned designs have a narrowband frequency response restricting their functionality. Generally, in an MIM cavity based absorber that is based on reflected/transmitted light cancellation, near zero reflection can be obtained in the vicinity of a specific narrow frequency range. For an optically thick reflecting layer, near zero reflection is equivalent to near unity absorption. The use of an unpatterned metal-insulator (MI) pair multilayer design is another strategy that was recently proposed and several recent studies have been conducted to obtain ultra-wideband (UWB) light absorption from these multilayers [17–20]. However, in these designs the light is absorbed in the middle metal layers (inside the cavity) and it is inaccessible for the outside object. Therefore, these designs cannot be efficiently employed in some applications, such as sensing. Moreover, most of them efficiently operate in a specific light polarization, losing their effectiveness in other polarization angles. In one of the pioneer works, in 2011, Aydin *et al.* proposed a subwavelength MIM stack with nanostructured top silver film composed of crossed trapezoidal arrays, achieving an average absorption of 71% within the visible frequency regime (400–700 nm) [21]. Other subwavelength geometries for the top layer were then proposed, but not all met the requirements for an ideal perfect absorber. Examples include, square [22–24], disc [25,26], and ring [27] arrays, as well as structures with sharp tips or grooves [28,29]. Essentially, in designing a perfect absorber several factors should be considered. Firstly, to obtain UWB absorption in a MIM stack, two general considerations need to be satisfied; 1) the plasmonic top layer geometry that supports multi-mode resonances needs to obtain a broad overall absorption, and 2) the insulator layer with a suitable thickness and refractive index to obtain the phase condition $\Delta\Phi \square 1$ v. To obtain a multi resonant response, several strategies have been employed for the design of a top layer patch. Using a multi shaped/sized architecture is one the most common methods to obtain ultra-broadband light absorption. In this configuration, different sized nanopatch resonators with different resonance frequencies are brought together and the superposition of these narrow peaks produces the overall broad absorption response. Moreover, some studies have proven that the existence of sharp corners in the design can ensure broad light absorption. An alternative option is to use elongated shapes (e.g., rectangular or ellipse) where elongation of the geometry in one direction can extend the light absorption toward longer wavelengths. However, this introduces a new complication as the light absorption is sensitive to the polarization. Unlike radially symmetric shapes such as nanoparticles and nanodiscs, which have infinite-fold symmetry and are insensitive to incident light polarization, elongated ones' response is sensitive to incoming light polarization.

In the present study, we propose an optimized lattice arrangement for an ultra-broadband light absorber design that produces a near-perfect polarization independent of the shape of the top metallic patches of the absorber. This design has the ability to retain its high absorption response, not only for transverse electric (TE) and transverse magnetic (TM) waves, but also for any arbitrary polarized light. In other words, by using this unit cell configuration both the bandwidth and polarization insensitivity attributes of the plasmonic design can be satisfied. In the paper, we first study the impact of the top patch geometries on the response of the absorber. The functionality of the structure under different polarization and incidence angles is then examined. Finally, the numerical results are supported by the fabrication and characterization of the proposed design. The findings of this paper are highly relevant in a

Optics EXPRESS

variety of applications where both polarization insensitivity and absorption bandwidth are required for the functionality of plasmonic absorbers.

2. Results and discussion

Figure 1(a) shows a top view of the design of the plasmonic unit cell. The structure was comprised of an MIM stack with a bottom titanium (Ti) layer, an aluminum oxide (Al_2O_3) spacer, and a top gold (Au) layer as shown in the Fig. 1(b). The top layer nanoresonant unit was fabricated with an elliptical design with minor and major diameters of D_1 and D_2, respectively. The unit cell dimensions were fixed at $P_x = 210$ nm and $P_y = 210\sqrt{3}$ nm, as shown in Fig. 1(a). As depicted in the scanning electron microscopy (SEM) image of the fabricated design [Fig. 1(c)], the periodic arrangement of these nanostructures formed the proposed metamaterial absorber. The spacer and top layer patch thicknesses are denoted by t_S and t_T.

The bottom layer thickness (t_B) was kept at 100 nm which is much thicker than the penetration depth of gold within the visible range. Therefore, transmission is nearly zero and absorption can be calculated utilizing the $A = 1 - R - T = 1 - R$ formula in which R denotes the reflected light from the structure. In the first step, the geometries of the structure should be optimized to ensure efficient excitation of the cavity modes inside the MIM design. Coupling of the surface plasmons at the upper and lower metal-dielectric interfaces can be effective provided that the dielectric spacer thickness is thin enough. On the other side, this layer should not be so thin that the reflective response of the bottom layer becomes dominant. The thickness of the spacer was optimized at 20 nm to get perfect light absorption over a broad frequency regime. Another factor that influences the MIM absorption response is the top layer thickness. The appropriate assignment of the top layer thickness should provide a tradeoff between reflection from the surface and the cavity modes resonance strength. According to these criteria, absorption over 0.9 within our desired frequency range was obtained by setting the top layer thickness at 60 nm.

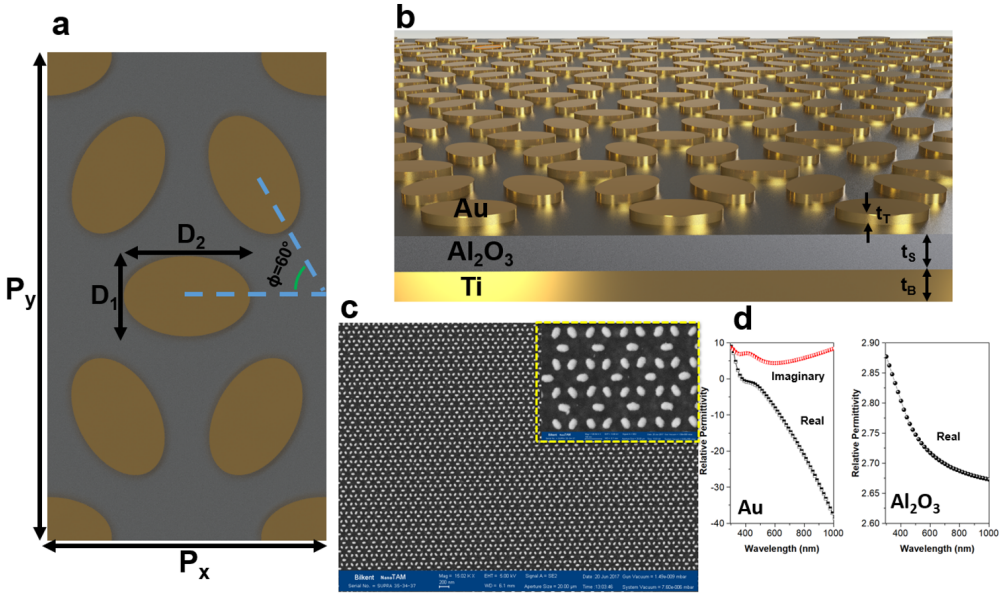


Fig. 1. Illustrative representation of the (a) unit cell, (b) cross section of the MIM design, (c) SEM image of the fabricated structure (the inset shows the magnified version of the design), and (d) the extracted relative permittivity values for the Au and Al_2O_3 layers.

Optics EXPRESS

To provide insight into the impact of these geometrical parameters on the MIM performance, a commercial finite-difference time-domain (FDTD) software package (Lumerical FDTD Solutions) [30] was employed. In our simulations, the structure was excited with a plane wave (in our desired polarization and angle of incidence) and a monitor recorded the reflected light off the surface. After performing spectroscopic scans using a V-VASE ellipsometer on deposited films of gold and alumina on different Si substrates, the permittivity values for these films were extracted using Drude-Lorentz and Cauchy models, respectively. The results are plotted in Fig. 1(d). The values for the physical dimensions of the spacer layer and top metal patch thicknesses of the proposed design were set at the above mentioned values. We conducted a sweep over the different combinations of the D_1 and D_2 values. As shown in Figs. 2(a)-2(d), the absorption of the structure was stronger for the larger values of D_1. Moreover, for a fixed value of D_1, the absorption upper edge experienced a red shift for larger values of D_2. In other words, the increase in the aspect ratio (defined as D_2/D_1) of an elliptic plasmonic structure increased the absorption capability of the structure for longer wavelengths. This is expected for an elongated design. Unlike radially symmetric designs, elongated geometries can support multiple resonance modes corresponding to their major and minor axes. The resonance wavelength of each of these modes is related to the physical dimension of these units where the increase in the dimension of the design extends its absorption peak toward longer wavelengths. A better qualitative comparison can be made by taking 0.9 as the threshold of near-perfect light absorption. For the case of D_1 = 30 nm, the response was improved for larger aspect ratios, however, the absorption capability of the design was not promising. This response was stronger for the case of D_1 = 40 nm where the absorption was retained above 0.9 in a wavelength range of 300–875 nm. For larger values of D_1, the upper absorption edge was shifted slightly toward longer wavelengths but the lower edge also moved to longer λ values. It should be noted that, as the value of D_1 increased, the nanopatches moved closer and the fabrication complexity of the design was also increased. To reveal the mechanism responsible for the light absorption in this MIM configuration, we have provided the contour plot for electric (E) and magnetic (H) fields in two different wavelengths, 420 and 680 nm, where the excitation light polarization was along the x-direction. As seen in Fig. 2(e), the E field distribution shows a dipole behavior for both wavelength values, but in the 420 nm case, the field was distributed through the walls of the patch while for a longer λ, this distribution appeared as hot spots at the metal-insulator interface. Previous studies have demonstrated that the periodic arrangement of plasmonic metal nanostructures, with a periodicity comparable with the excitation light wavelength, can support collective resonances of the lattice by the diffractive coupling of individual localized surface plasmon resonance modes (LSPRs), and the physical origin of this is attributed to Fano interference [31–35]. Therefore, it was expected that the top metal nanopatch was responsible for the absorption in the shorter wavelengths. Moreover, looking at the magnetic field profiles shown in Fig. 2(e), the magnetic field distribution was fundamentally different for long and short wavelengths. At the shorter wavelength of 420 nm, the magnetic field was confined between the resonators and for the 680 nm incident light the distribution was located beneath the nanoresonant patch (inside the cavity). As explained in previous studies [25,36], the confinement of the magnetic field in the area between adjacent nanopatches demonstrates the excitation of propagating surface plasmon (PSP) modes. These modes propagate at the interface of the continuous Ti and alumina layers and dissipate their power at the highly dispersive Ti metal layer. This can be verified by observing the magnetic field distribution of the structure for the shorter 420 nm wavelength case. The magnetic field plot indicates that large currents were flowing along the lower metal layer between the patches. Since the lower layer was Ti, which is very lossy and highly dispersive, a significant fraction of the incident energy was dissipated in the Ti layer. However, at the longer wavelength, the magnetic field confinement at the area below the nanopatch (between the top and bottom metals) supported its localized nature. That is, the mechanism responsible for the light absorption in the longer

Optics EXPRESS

wavelengths was related to the excitation of the localized surface plasmons (or gap surface plasmons) inside the cavity. To evaluate the ex- istence of the above-mentioned phenomena, the amount of absorbed power was calculated at the top nanopatches and the bottom Ti layer using a three-dimensional (3D) monitor, as shown

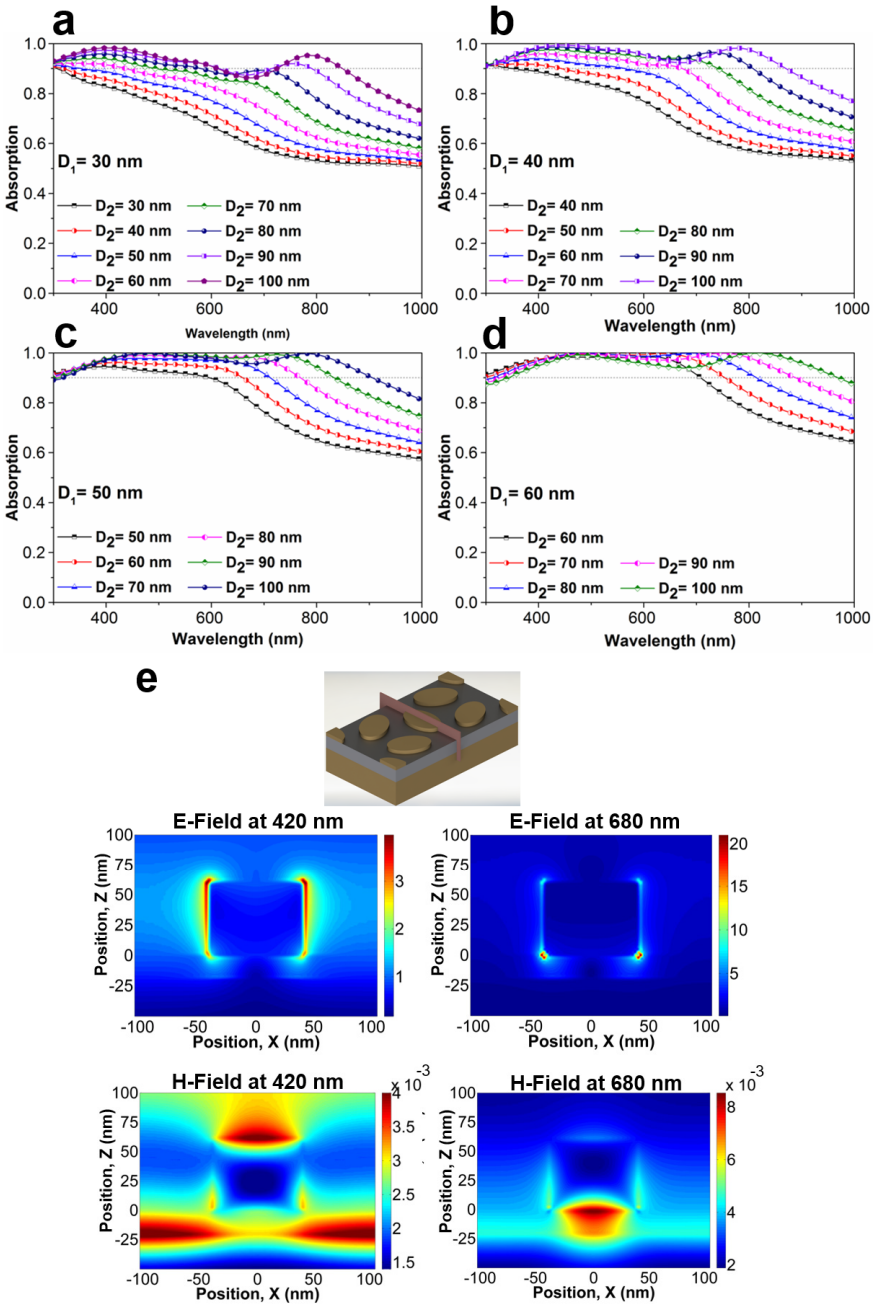


Fig. 2. Impact of the ellipse diameters on the absorption spectra of the MIM design for four different cases for D_1 of (a) 30 nm, (b) 40 nm, (c) 50 nm, and (d) 60 nm. (e) The corresponding electric and magnetic field distribution across the MIM design for two different wavelengths of 420 and 680 nm. The units of E and H fields are V/m and A/m, respectively.

Optics EXPRESS

in Fig. 3(a). As this panel clearly demonstrates, the absorption in short wavelengths occurred at both the bottom continuous Ti layer and top gold nanopatches. Therefore, as discussed previously, the absorption in shorter wavelengths is the result of two mechanisms; (1) the collective resonances of the lattice by the diffractive coupling of individual LSPR modes in the top nanoresonant patch, and (2) the excitation of PSP modes in the interface of the continuous Ti bottom layer and alumina spacer. However, in the longer wavelength range, the absorption was dominated by the bottom lossy Ti layer. By considering the highly confined nature of the magnetic field for longer wavelengths, this absorption was due to the excitation of localized gap surface plasmons inside the cavity. In this case, considering that Ti is much more dispersive compared to the gold layer, most of the light was absorbed in the bottom layer. Therefore, the superposition of all of these mechanisms provided a near-perfect absorption throughout an ultra-broadband frequency range. A better understanding of the origin of the cavity resonance modes can be obtained by probing the near field enhancement (NFE) in the metal-insulator interface plane, as depicted in Figs. 3(b)-3(d). To get the NFE intensity values for different structures, we used point monitors in our simulations. At the interface of the top metallic patches and the alumina spacer, we placed 6 different point monitors around each elliptical patch and averaged all the intensity values by $|E|^2$. The arrangement of these point monitors (that are displayed by red points) in the unit cell are shown in the inset of Fig. 3(d). Afterwards the top nanopatch resonators were removed and the background intensity ($|E_0|^2$) was calculated for the structure (made of the bottom metal with the spacer coated on it). Finally, the NFE values were calculated as $\frac{|E|^2}{|E_0|^2}$. Considering both the fabrication complexity and optical performance of the structure, the values $D_1 = 40$ nm and $D_2 = 80$ nm were chosen as the target design for the rest of the paper.

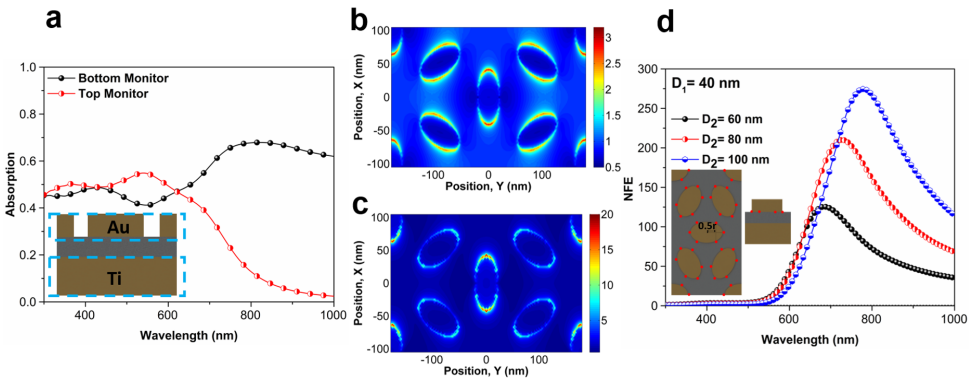


Fig. 3. (a) Amount of absorbed power in bottom and top monitors located in the positions shown in the inset of the panel. The electric field distributions in the interface plane of the top metal and insulator for two different wavelengths of (b) 420 nm, and (c) 680 nm. (d) The NFE values for the three structures with different aspect ratios. The inset shows the position of the point monitors.

Figures 3(b)-3(c) show the E field distribution at the interface plane for two different wavelengths. As clearly revealed in this panel, although the E field distribution was similar for both cases, the intensity of the light was stronger for the longer wavelength light. To understand the impact of the elliptical aspect ratio on the cavity modes resonances, the near field distribution was recorded for three different cases with different aspect ratios, and plotted as a function of the wavelength of the incident light in Fig. 3(d). According to these results, the near field distribution showed a sharp enhancement after 550 nm and reached a strong peak in the wavelength range of ~700–800 nm, before exponentially declining toward the near infrared (NIR) region. This is in line with our previous explanations that cavity

Optics EXPRESS

resonance modes are activated for longer wavelengths. Moreover, these findings suggest the reason for the absorption bandwidth enhancement for larger aspect ratio features. As this ratio enlarges, the peak position experiences a red shift, and this approach is effective in achieving ultra-broadband light absorption. If this ratio is too large, the activation of the cavity modes moves to longer wavelength values and, therefore, a gap will be created between the top metal resonant modes and the cavity ones. This is why we observed a dip for the cases with $D_2 = 100$ nm, as depicted in Figs. 2(a)-2(d). Therefore, a successful design should include the optimum series for both of these resonance modes.

We examined the impact of the unit cell arrangement on the MIM cavity absorption for different incident light polarizations by setting the values of D_1 and D_2 to 40 and 80 nm, respectively. To better understand the proposed unit cell arrangement, our proposed unit cell was compared with two commonly used polarization insensitive designs; triangular and honeycomb lattices. As mentioned earlier, the main approach in imposing polarization insensitivity on the absorption behavior of a configuration is to use infinite-fold symmetric shapes as the top nanopatch structure (i.e., nanoparticles and nanodiscs). However, this imposes a restriction on the choice of the nanoresonant unit, and its importance was discussed in the previous section. Moreover, most of the designs, such as rectangle, ellipse, and other similar elongated designs, can only offer two fold symmetry on their major and minor axes. Therefore, these provide independent polarization for only transverse magnetic, TM ($Ø = 0°$) and transverse electric, TE ($Ø = 90°$) polarized lights. This can be better clarified by looking at the illustrative representation provided in Fig. 4. If four different polarizations ($Ø = 0°, 30°, 60°,$ and $90°$) are shined on the absorber, the absorption capabilities for normal incidence can be examined. To make it visually clearer, instead of the source, we rotated the structure by the above mentioned angles. In other words, the light polarization was kept constant in the x direction, but the sample was rotated. The unit cell (in the Cartesian x-y coordinate) that the light periodically sees is shown in the corner of each shape. As can be clearly seen from this figure, for both the triangular and honeycomb lattices, the unit cells are the same for both the $0°$ and $90°$ polarization angles. However, these unit cells were not retained for the $30°$ and $60°$ polarizations. This is the reason why such lattice arrangements cannot impose polarization insensitivities in the light absorption for all polarization angles ($0°<Ø<90°$). Unlike these architectures, our proposed cell arrangement keeps its unit cell intact for all four angles. It is noteworthy that in the 0° polarization case, the electric field was along the major axis of the central elliptic light absorption for all polarization angles ($0°<Ø<90°$), while for the 90° polarization case, it was parallel to its minor axis. However, in the 0° rotation case, the electric field was parallel to the major axis of the two elliptical metallic patches [one in the center and one in the corner (4 × 1/4)], while it was mostly aligned with the minor axis of the other four ellipsoids which were located around the center. When we rotate the unit cell by 90°, the E field was aligned with the minor axis of the two elliptical patches, nevertheless for the other four units the field was mostly aligned with the major axis of the ellipses. Consequently, the 0° and 90° rotations exhibited the same net interaction with the electric field of the incident light. Therefore, this proves that by arranging the resonator units in the proposed fashion ensures polarization independence regardless of the shape of the patch unit. This was evaluated with FDTD simulations are shown in Fig. 5(a). This figure shows that the structure provoked an almost absolute polarization insensitivity for all polarizations of the incoming light where the absorption amount throughout the whole visible frequency range was near unity. Another feature that defines the functionality of the MIM cavity is its omni-directionality. Numerical simulations were employed to evaluate the absorption capability of the stack upon excitation with different angles. Figures 5(b)-5(c) reveal the absorption response of the structure for oblique incidence angles ($0°<θ<50°$) for TM and TE polarized lights. As illustrated in this figure, the visible

Optics EXPRESS

light absorption remained almost above 0.85 in all angles for both the TM and TE polarizations. As the thicknesses of all three layers were subwavelength, the phase

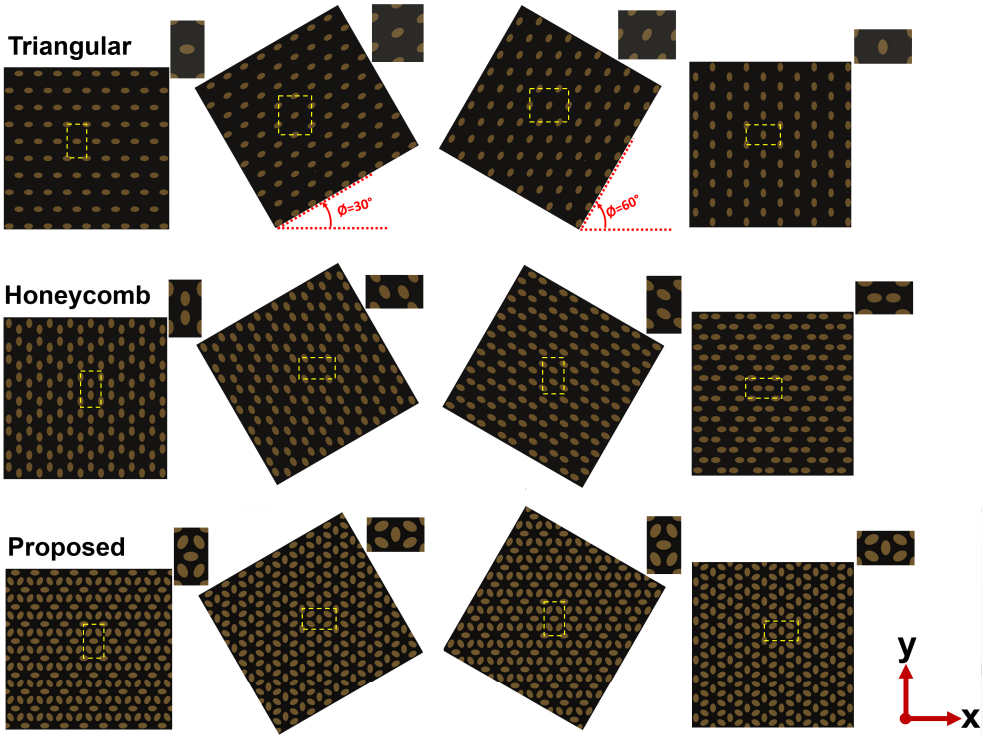


Fig. 4. Equivalent unit cells of the triangular, honeycomb, and proposed designs for different light polarizations.

charge accumulation was almost the same as the normally incident light and, therefore, the absorption capability of the cavity was maintained for the other angles of incidence.

To evaluate our numerical findings, the proposed structure was fabricated [as shown in Fig. 1(c)] and optically characterized under different polarizations and angles of incidence. The fabrication route of the proposed design can be briefly explained as follows. First, the Si substrate was cleaned using a standard cleaning process with Pirahna and Hf solutions. Afterward, a 100 nm thick Titanium layer was deposited on top of these substrates using a thermal evaporator. The Al_2O_3 depositions were carried out at 250°C in an atomic layer deposition (ALD) reactor (Cambridge Nanotech Savannah S100) employing an $Al(CH_3)_3$ solution as the deposition precursor. The pulse and purge times were 0.015 and 10 s, respectively. The growth rate was found to be 1.01 A° per cycle and the number of cycles were chosen such that the overall thickness of the alumina was 20 nm. Electron beam lithography (RAITH E-Line Plus) was employed to fabricate the nanoresonant ellipsoids. First, a 250 nm 495 k PMMA resist was spin coated on top of the prepared structure. The electron beam exposure was then performed with a beam writer at an acceleration voltage of 30 kV, e-beam spot size of 5 nm, and a 350 pA beam current. To obtain an ellipsoid structure with different major and minor axes dimensions, we performed a dose study on the sample. The major axis dimension was tuned with the change of line length and the width was controlled by the amount of exposure dose. Increasing the dose factor increases the fabricated design dimensions. Finally to obtain our desired dimensions, we used single pixel line exposure with a dose of 3000 pC/cm. After the exposure, the samples were developed at room temperature utilizing a MIBK:IPA (1:2) solution for 2 min followed by an immersion in IPA

Optics EXPRESS

for 30 sec. At the last step, the deposition of the 60 nm gold layer was conducted using a thermal evaporator and the samples were left for the lift off process over night.

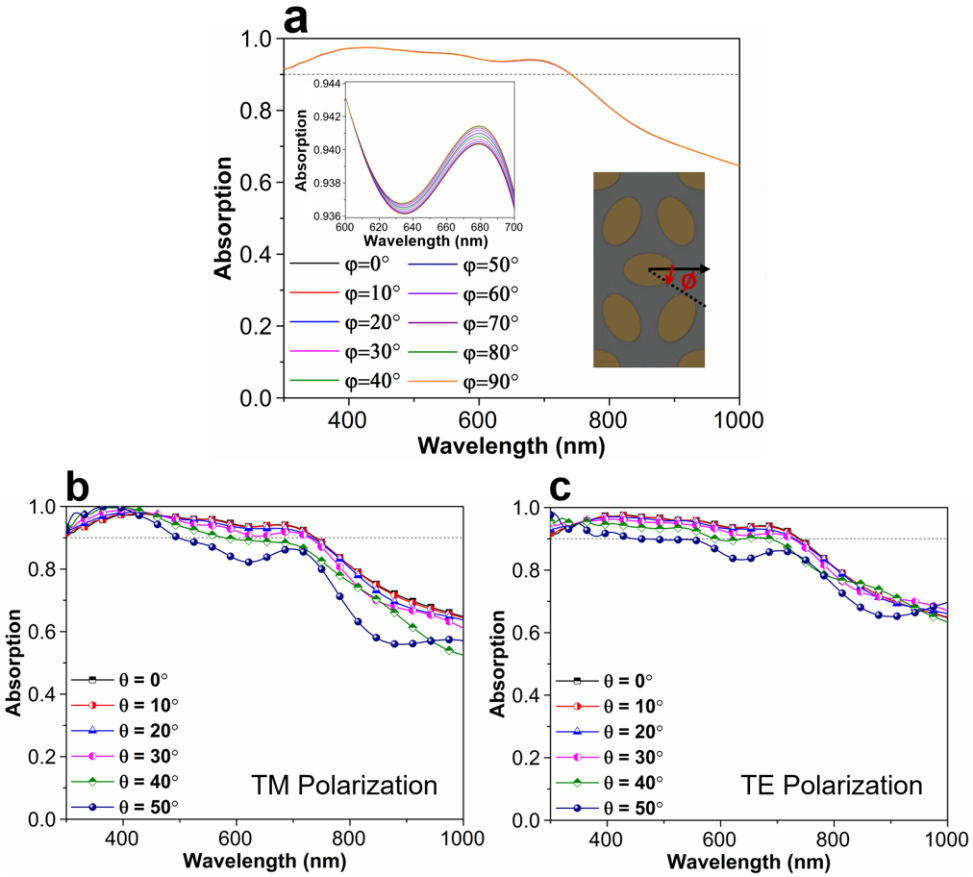


Fig. 5. The simulated absorption spectra of the MIM structure upon excitation with (a) different light polarizations, and different angles of incidence for the (b) TM and (c) TE polarizations.

To obtain the optical characterization of the stack, the normal reflection measurements for the wavelength range of 300 to 1000 nm were carried out using a homemade reflection measurement setup. This consisted of a Halogen illuminator as the source, connected to a microscope (series with a polarizer) and the output was illuminated perpendicularly to the sample. The reflected light from the microscope was also fed into a Newport OSM2 spectrometer in which the data was collected by interfacing the spectrometer with a personal computer. The oblique incidence reflection measurements were conducted by employing a J.A. Woollam Co. Inc. V-VASE ellipsometer for different polarizations and incidence angles. Figure 6(a) depicts the response of the structure upon excitation with different incident light polarizations ranging from 0° to 90° in steps of 15°. The response of the system was almost independent of the polarization of the light, wand was in agreement with our numerical findings. Moreover, the proposed MIM structure had the ability to retain its high absorption response for the whole of the visible frequency range. To provide a better qualitative comparison, the averaged absorptions of the stack for different angles of incidence were calculated and are plotted in the inset of Figs. 6(b) and 6(c). The averaged absorption of the structure remained above 0.88 for all angles of incidence and polarizations.

Optics EXPRESS

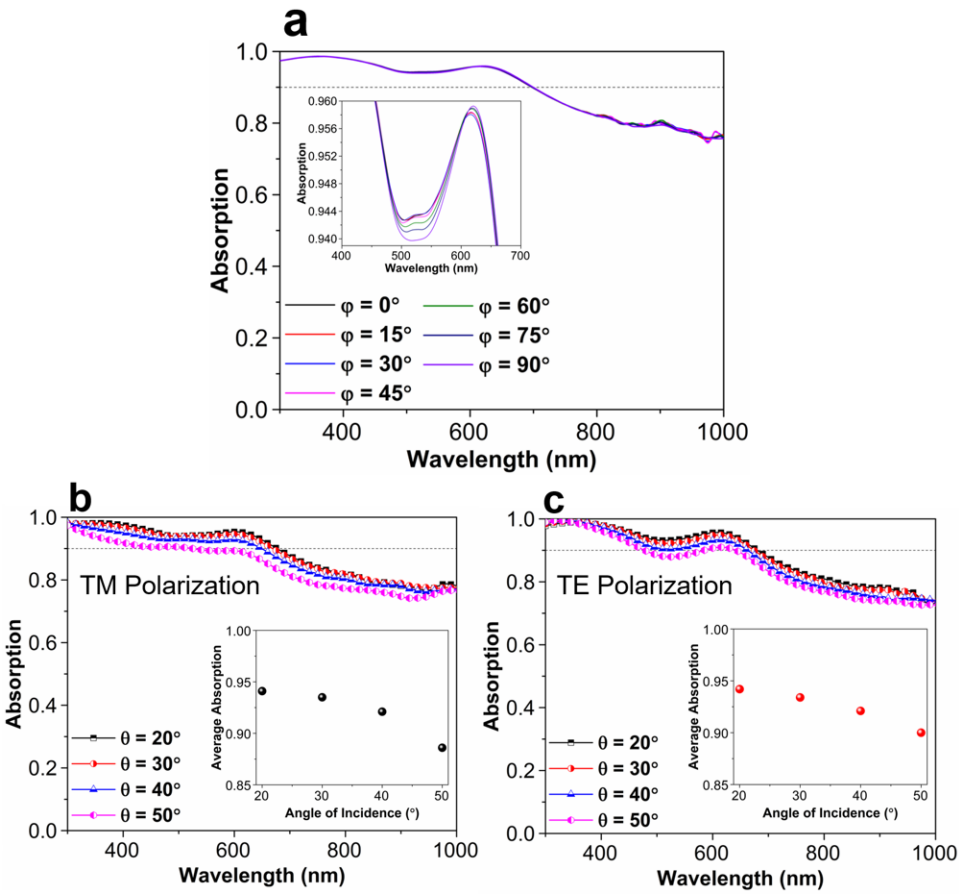


Fig. 6. The absorption spectra of the fabricated MIM structure upon excitation with (a) different light polarizations, and different angles of incidence for the (b) TM and (c) TE polarizations. The inset shows the averaged visible light absorption values of the design.

3. Conclusion

In summary, in this study we designed, fabricated, and characterized an ultra-broadband nearly perfect MIM absorber with an almost absolute polarization insensitivity. First, we examined the impact of the top metal patch on the absorption bandwidth of the design. Our findings showed that for more elongated designs, the absorption capacity of the system is improved. Moreover, to ensure polarization insensitivity in the absorption response, we proposed an optimum arrangement of the cells to obtain an efficient structure. The results presented here are useful for the design of future high performance devices for a wide range of applications based on broadband and narrowband absorbers where both near-perfect absorption and polarization insensitivity are required.

Funding

Scientific and Technological Research Council of Turkey (TUBITAK); DPT-HAMIT Project Nos. 113E331 and 109E301.

Acknowledgment

One of the authors (E.O.) also acknowledges partial support from the Turkish Academy of Sciences.

139.179.98.142 {ts '2017-11-15 01:10:28'}